

Investigating the Thixotropic Behaviour of Tremie Concrete Using the Slump-flow Test and the Material Point Method

Christopher Wilkes^a, Krishna Kumar^b, Giovanna Biscontin^a

^aDepartment of Engineering, University of Cambridge, Cambridge CB2 1PZ, United Kingdom

^bDept of Civil Architectural and Environmental Engineering, Cockrell School of Engineering, University of Texas at Austin, Texas, USA

Abstract

This paper presents a new thixotropic model integrating the Papanastasiou-Bingham model with thixotropy equations to simulate the flow behaviour of Tremie Concrete in the Material Point Method framework. This study investigates the effect of thixotropy on the rheological behaviour of fresh concrete by comparing field measurements with numerical simulations. The comparison yields new insights into a critical and often overlooked behaviour of concrete. A parametric study is performed to understand the effect of model parameters and rest-time on the shear stress response of fresh concrete. The Material Point Method with the Papanastasiou-Bingham model reproduces Slump-flow measurements observed in the field. The novel model revealed a decline in concrete workability during the Slump-flow test after a period of rest due to thixotropy, which the physical version of the test fails to capture. This reduction in workability significantly affects the flow behaviour and the effective use of fresh concrete in construction operation.

Keywords: Tremie Concrete, Numerical Modelling, Concrete Testing, Rheology

1. Introduction

Tremie Concrete is widely used to construct bored piles and diaphragm walls for its superior post-hydration compressive strength and high level of workability. The term workability is often used interchangeably with consistence; however, both terms are useful descriptors of the relative mobility or the ability of fresh concrete to flow [1]. The requirements for the use of Tremie Concrete in deep foundations includes its ability to flow around obstacles like a congested reinforcement cage and freely through a pipe, thereby, needing a high degree of consistence. When left undisturbed, tremie concrete stiffness will progressively increase during the dormant period of the hydration reaction [2, 3], leading to a reduction in the ease with which it can flow. Fortunately, the loss of mobility due to the increase in stiffness can be recovered with an application of stress, so long as the applied stress is significant enough to break down the hydration byproducts causing the elevated strength [3]. The temporary reduction in concrete mobility that can be alleviated by stress application is referred to as thixotropy.

Thixotropy poses a severe issue in the construction industry as changes to flow behaviour can hinder the ability of new concrete to mix with the existing concrete, thereby creating weak interface planes [2]. Furthermore, thixotropic changes in concrete could prevent concrete from flowing freely around reinforcement bars during long pile casting operations [4].

Increasingly, the suitability of a concrete mix design is examined through numerical analysis of the construction operation [1, 5, 6, 7, 8]. However, the most popular approach of modelling uses Computational Fluid Dynamics based numerical methods which encounter difficulty when simulating

thixotropic behaviour due to the Eulerian frame of reference. The Material Point Method (MPM) [9, 10] is an emerging numerical method capable of simulating large deformation and time-dependent material allowing for the simulation of thixotropic concrete.

The objective of this paper is to develop a comprehensive thixotropic model in the Material Point Method (MPM) framework, to accurately capture the history-dependent nature of the flow behaviour of Tremie Concrete. This paper provides unique insights into the history-dependent nature of Tremie Concrete and the associated flow response by exploring the challenges associated with testing and simulating thixotropic concrete.

2. Flow Behaviour

2.1. Slump-flow test

The Slump-flow test [11] (fig. 1), is an empirical test that quantifies a concrete's flow behaviour by measuring Slump flow spread (SF) - the distance concrete spreads before stopping when emptied from a rising cone [12]. Even in its simplicity, the SF test is able to capture a snapshot of concrete flow behaviour at a single point in time, however, the test has drawn criticism for its inability to observe or provide insight on the behaviour of concrete following a period of rest [13, 14]. The SF of a Tremie Concrete is typically in the range of 500 mm to 600 mm [12], although, in practice, concretes with a SF as low as 450 mm or as high as 650 mm are also considered acceptable [1]. Recent analysis of concrete SFs [15, 16, 17] found the Bingham rheological model is able to accurately describe the flow behaviour of fresh concrete [13, 14].

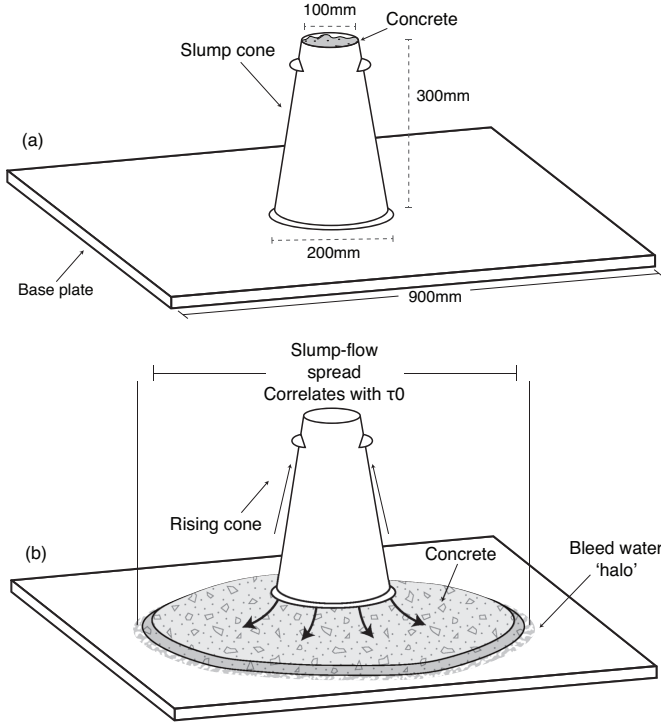


Figure 1: a) Slump-flow test apparatus in accordance with BS EN 12350-8:2019. b) Representation of a typical Slump-Flow spread (SF).

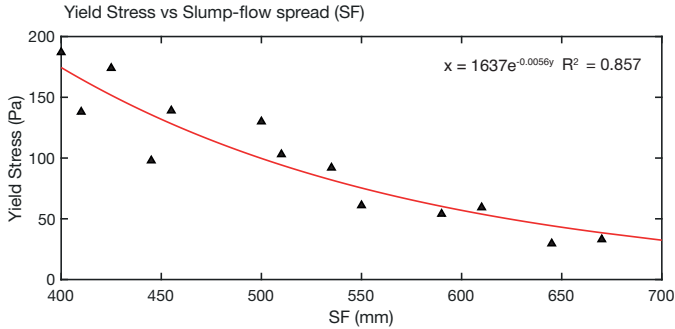


Figure 2: Experimental correlation between dynamic yield stress and slump flow (redrawn after [13, 14]).

A material's rheology provides a quantifiable description of its flow properties. The Bingham rheological model [18] is represented as:

$$\tau = \mu\dot{\gamma} + \tau_0, \quad (1)$$

where τ represents the shear stress, τ_0 the yield stress, μ the plastic viscosity and $\dot{\gamma}$ the shear rate. The yield stress, τ_0 , represents the initiation force needed to commence flow but both the yield stress and plastic viscosity μ control the flow behaviour. In the Bingham model, materials experiencing stresses below a critical yield stress behave akin to rigid bodies with viscoelastic effects, whilst stresses that exceed the yield criteria cause the material to flow and behave as a viscous liquid [19].

SF measurements and rheological models such as the Bingham model, are fundamental to validating numerical methods. Rheological measurements obtained from a rheometer can be

input directly into a numerical model and the associated flow behaviour, represented by an SF, observed and compared with expectations. Thus, SF results paired with rheological measurements not only provide a way to validate a numerical model, but also a pathway to overcome the limitations of verifying the construction operation.

Figure 2 shows the experimental correlation between yield stress derived from rheometer and SF. The SF is observed to increase exponentially as the yield stress decreases [15, 16, 17]. When the shear stresses generated during the slump flow test are lower than the yield stress of the concrete, the flow stops [5]. Thus, any change in yield stress will inherently influence the distance at which the flow stops, creating the yield stress and SF relationship demonstrated in Figure 2.

Plastic viscosity also impacts the flowability, however, its influence on the SF spread is considered less significant than that of the yield stress as no strong correlations have been established with the stopping distance of the concrete spread. The plastic viscosity does effect the rate at which concrete spreads [19, 20, 5, 13, 14], so an increase in plastic viscosity increases the time taken for concrete to stop spreading, referred to as SF-Time by EFFC and DFI [1]. However, it is worth noting that Deeb et al. [21] and Roussel and Gram [5] showed that the speed at which the cone is raised influences the spreading rate, without changing the final SF [22, 23]. The relation between SF-Time and plastic viscosity may depend on the variance between different operators raising the cone at different speeds, within the Slump-Flow test standard [11]. To validate a rheological model, it is important to compare against the final run-out distance rather than the SF time. The SF time should not be used solely to confirm if a numerical model is reliable.

Where the input values for a simulation are taken from field measurements, the accuracy of a Slump-Flow simulation can be judged largely by considering the level of agreement between the simulated SF and field SF, as the yield stress/ SF relationship is subject to less controversy and user-variance. Although the yield stress/SF correlation is better than that of plastic viscosity/ SF-time, there is still variance in the behaviour of concrete as the yield stress changes at rest due to thixotropy; which cannot be easily captured by the Slump-Flow test. Thus, the variability in the yield stress and the impact thixotropy has on the Slump-flow test must be evaluated in order to use SF as a validation method for time-dependent concrete flow behaviour.

2.2. Thixotropy

The yield stress of a cement-based material like concrete originates from the micro-structure of cement particle-particle networks through colloidal interactions or direct contact between cement particles [24]. This micro-structure can sustain a certain amount of stress before it is broken down and starts to flow. In the Bingham model of concrete, the resistance to flow due to the micro-structure is defined as the yield stress [2]. At rest, this micro-structure will continue to build up due to colloidal flocculation and formation of calcium silicate hydrate (CSH) bridges between particles as a result of partial hydration of cement [3], resulting in increased yield stress [25], leading to thixotropy. When sufficient shear force is applied, the

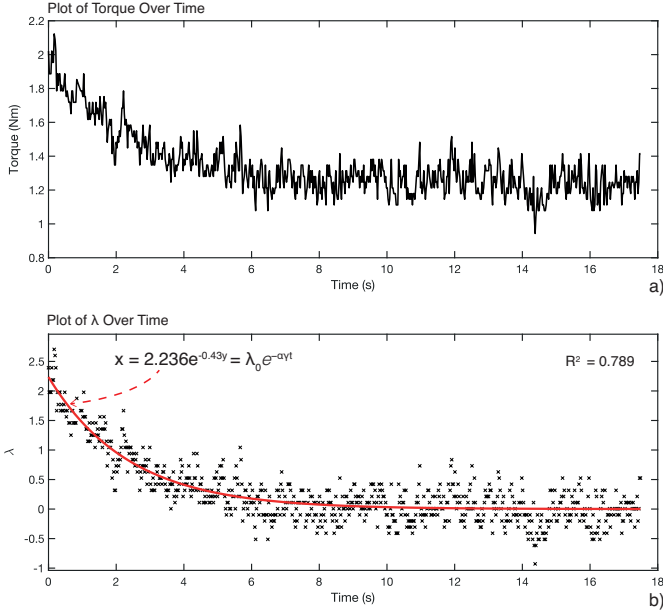


Figure 3: a) Evolution of torque with time, measured by a rotating vane submerged in Tremie Concrete, with a shear rate of 12.43 s^{-1} . Torque decaying over time to a constant average. b) Evolution of λ over time with a fitted exponential curve. Data provided by internal communications with ARUP.

micro-structure will begin to break down, causing the elevated yield stress to dissipate to a constant yield stress upon which no further breakdown of the structure is possible. The temporary increase in yield stress after a period of rest is referred to as the ‘static’ yield stress, while the constant yield stress observed once the elevated level has dissipated is referred to as the ‘dynamic’ yield stress [24].

Roussel [2] proposed a series of equations to characterise the influence of thixotropy on yield stress. Incorporating a flocculation state λ in eq. (1) gives:

$$\tau = \mu\dot{\gamma} + (1 + \lambda)\tau_0, \quad (2)$$

$$\frac{\partial \lambda}{\partial t} = \frac{A_{thix}}{\tau_0} - \alpha\lambda\dot{\gamma}, \quad (3)$$

where A_{thix} is the restructuring rate at rest and α is the destruction parameter (typically of the order 0.01) [26]. Considering the rate of build-up of the micro-structure, A_{thix} , is relatively slow compared to the rate of destructuration, as reported by [27, 2], eq. (3) becomes:

$$\frac{\partial \lambda}{\partial t} = -\alpha\lambda\dot{\gamma}. \quad (4)$$

integrating eq. (3) with respect to time, we get:

$$\lambda = \lambda_0 e^{-\alpha\dot{\gamma}t}, \quad (5)$$

where, t is time spent at a particular shear rate and λ_0 is the original flocculation state. The three thixotropic parameters (λ , α and A_{thix}) can be computed by measuring the torque required to shear a rested concrete.

Figure 3a shows a gradual decay of observed torque with time for a Tremie Concrete using an ICAR [28] rheometer at

a site within the United Kingdom. Coaxial rheometers such as the ICAR [28] use a rotating vane submerged in a cylinder filled with concrete to measure torque. Bingham parameters are then derived from the torque and rotational velocity using the Reiner-Riwlin equations [29, 30]. Incidentally, the observed torque, T , will gradually decay from an elevated initial measurement to a stable value. In fig. 3a, torque reduces from approximately 2 N m to a stable value of 1.25 N m after shearing (rotation of the vane) for approximately 10 s. The reduction from 2 to 1.25 N m, assuming a constant rotational velocity of the vane, indicates the transition from static yield stress to dynamic yield stress. The thixotropic parameters of the Bingham model can be calculated using the apparent shear stress, defined as a function of the observed torque T , radius r and height h of the vane. The apparent shear stress is measured in a rheometer as:

$$\tau_{apparent} = \frac{T}{2\pi r^2 h} = \mu\dot{\gamma} + (1 + \lambda)\tau_0. \quad (6)$$

From eq. (6), $\tau_{apparent}$ can be used to calculate a flocculation state λ for a given apparent shear stress. Thus, by taking $\tau_{apparent}$ at different time intervals and using it to calculate the corresponding flocculation state of the concrete, a λ /time plot can be generated as shown in fig. 3b. At the maximum λ , the elevated static yield stress can be calculated as:

$$(1 + \lambda)\tau_{0dynamic} = \tau_{0static}. \quad (7)$$

Despite noisy data measured in a rheometer, an exponential best-fit curve can be applied to the λ /time plot (fig. 3b) to generate an approximation of α . The coefficient of the exponent, 0.43, from fig. 3b is divided by the known constant shear rate, 12.43 s^{-1} , as per eq. (5), to yield an approximate α of 0.0358.

In the present study, an α of 0.01 is used for all concretes as the raw rheometer data for the examined concretes is unavailable. However, this value represents an α supported by Roussel [2].

The remaining thixotropic variable, A_{thix} , which represents the rate at which yield stress increases over time (Pa s^{-1}), can be calculated using the static yield stress in eq. (7):

$$A_{thix} = (\tau_{0static} - \tau_{0dynamic})/rt. \quad (8)$$

A_{thix} is used as a single value representing the thixotropic propensity of concrete, where a value of $A_{thix} > 0.5$ is considered to be highly thixotropic [2]. A_{thix} values greater than 3.0 for some Tremie Concretes were reported by [13, 14] for concrete with a rest time of 240 s. This represents a large increase in yield stress over a relatively short period. It is therefore reasonable to expect a significant decline in SF after a period of rest for highly thixotropic concrete, given such a large increase in yield stress. The difference in Slump-flow before and after a period of rest is written as ΔSF , where:

$$\Delta SF = SF_0 - SF_{240}. \quad (9)$$

with SF_0 and SF_{240} representing the SF measured following 0 s of rest and 240 s of rest respectively.

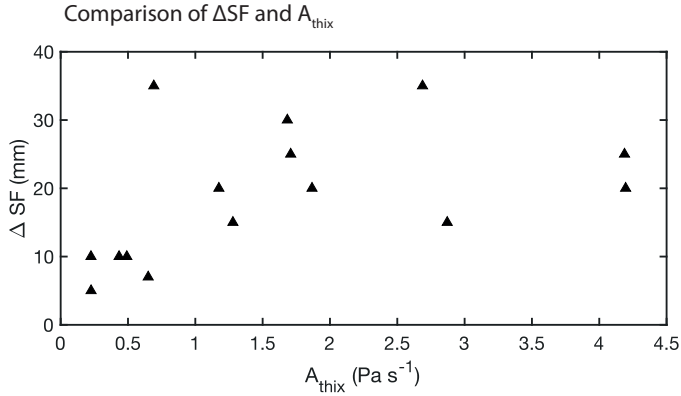


Figure 4: Comparison of change in SF at 240 s and 0 s (ΔSF) with A_{thix} . Created using data from [13, 14].

The comparison of slumps before and after 240 s for different concrete mixes, shown in fig. 4, indicates only small changes in SF despite large A_{thix} values [13], although a general pattern of increasing ΔSF with A_{thix} is observed, no confident trend can be identified. Upon further inspection, a mix with an A_{thix} of 2.87 resting for 240 seconds experienced a reduction in SF of only 15 mm despite an increase in yield stress of 688 Pa from an initial value of 130 Pa. Given the relationship between yield stress and SF shown in fig. 2, a high value of yield stress should result in a significantly reduced SF that is no longer within the acceptability limits for a Slump-flow test, clearly that did not occur in this case. This lack of SF reduction can be explained partially by the underlying relationship between yield stress and plastic viscosity created by mix designers to maintain stability at low yield stresses or low viscosities. To maintain stability, the yield stress of a low viscosity concrete would be increased, and vice versa. These alterations are conducted by altering the mix design, modifying fines or water content, or the use of additives. Thus, an elevated yield stress, relatively low viscosity concrete will not have the same SF/Yield stress relationship as in fig. 2. Nevertheless, given the significant effect yield stress has on SF, a decrease in SF of at least 100 mm would not be unexpected for an increase in yield stress as dramatic as 688 Pa.

The unexpectedly small ΔSF values shown in fig. 4 can be further explained by examining the experimental procedure used to gather the data. During the 240 s rest period, the concrete remains undisturbed in the cone on a base-plate. As the cone is not sealed on the base plate, bleed water from the concrete can accumulate at the base and seep out. The test standard BS EN 12350-8:2019 [11] specifies a maximum wait time of 30 s to avoid potential issues like dewatering, as any water at the base can reduce friction between the concrete and the base plate, leading to a larger SF. Kraenkel and Gehlen [13] also reported a 30 mm variation in SF within the allowable resting time, indicating potentially large inaccuracies. Some concretes in fig. 4 saw a 100% increase in yield stress in just 30 s of rest. Considering that BS-EN 12350-8:2019 [11] allows up-to 30 s rest before the cone is raised, it is conceivable that the concrete has already accrued some degree of thixotropy in the regular test that the SF_0 figures represent.

Hence, obtaining any meaningful thixotropy effects in a physical Slump-flow test can become highly challenging [13, 14, 31]. If the thixotropic behaviour of concrete is not correctly understood, issues of restricted concrete flow behaviour during the construction process could occur. Hence, the measurements of thixotropy can be of great importance in practice. Numerical models can minimise the variability of physical tests by allowing for greater control over all variables, creating an ideal testing situation, thereby offering unique insights into concrete flow behaviour by accurately considering the influences of thixotropy which are otherwise obscured by physical testing.

3. Materials and Methods

3.1. Numerical Model

The behaviour of fresh concrete is typically modelled as a continuum using Lagrangian methods [21, 32] or Eulerian Computational Fluid Dynamics (CFD) [1, 16, 5, 26, 33, 6]. De Schryver et al. [34] modified OpenFOAM® (Open Source Field Operation and Manipulation), a popular CFD solver, to incorporate time-dependent thixotropic concrete behaviour. However, at the time of writing the method remains unvalidated. A comprehensive review of numerical methods used in the modelling of concrete flow is presented by Rousset and Gram [5] with more recent model reviews presented by [7, 8]. Continuum methods are suitable for large scale problems but may struggle simulating less workable concrete where inter-granular relationships become more important. Discrete particle methods [32] or Smooth Particle Hydrodynamics [21] methods that represent concrete as individual particles capture the micro-scale behaviour accurately, however, these methods are computationally intensive and cannot always be scaled to the full field-scale. Hence, there is a need for continuum-based numerical methods capable of incorporating micro-structural laws in describing the macroscopic rheological response.

MPM [9, 10] offers a new hybrid Eulerian-Lagrangian approach that combines the Lagrangian benefits of point tracking with the Eulerian background grid for modelling large deformation problems with history-dependent materials [35, 36]. The MPM uses a background grid on which Lagrangian material points could traverse, thereby avoiding the need for frequent remeshing to avoid mesh distortion [37]. MPM has been used to successfully model large deformation [35], interaction [38], and history dependent materials [39] with a high degree of accuracy. In this study, MPM is used for the first time to model concrete flow behaviour.

The MPM involves taking a continuum body and discretising it into a finite set of material points, the tracking of properties at these points represents the Lagrangian portion of the hybrid approach. The Eulerian part of MPM comes from a background grid on which the momentum equation is solved. This background grid encompasses the entire domain of the problem. Typically, the MPM Eulerian background grid is a Cartesian domain of rectilinear elements. Each element is defined by nodes, usually at the vertices of the element unless otherwise specified. The material points carry the material properties, such as density, stresses, shear strength and viscosity, and are specified as

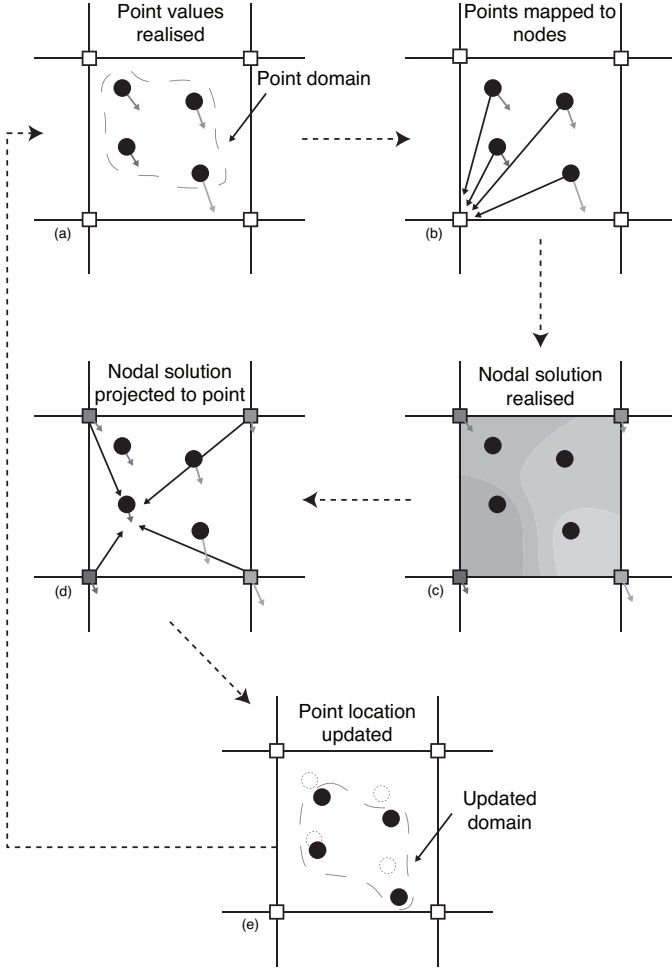


Figure 5: Schematic diagram of the material point algorithm, arrows represent material point properties (velocity, mass, etc.) a) Point values are initialised b) Point values are mapped to nodes c) The equations of momentum are solved on the nodes d) Updated Nodal values are projected back to points e) Point locations and states are updated.

an input. Figure 5 presents a schematic diagram of the MPM solution process. The shape-functions, which are derived from the position of the material points within the element, are used to map material point properties to the nodes, fig. 5a-b, [35]. The equation of motion is solved at the background mesh to find the current acceleration, with the element integration based on the material point locations [40], fig. 5c. The grid nodal acceleration and velocity values are mapped back to the points to update their velocities and positions using the same shape functions as before [41], fig. 5d. The stresses are computed at each material point using a constitutive model. Finally, the locations of the material points are updated based on the mapped velocity from the node as shown in fig. 5e. The mesh is reset at the end of each iteration, therefore, no permanent information is stored at the nodes.

3.1.1. Governing Equations

Neglecting the thermal effects, the governing equations for the MPM are derived from the standard conservation equations for mass and momentum, eq. (10) and eq. (11) respectively. Derivations presented here are based on work conducted by [10, 36, 35, 41, 42].

$$\frac{d\rho}{dt} + \rho \nabla \cdot \mathbf{v} = 0, \quad (10)$$

$$\rho a = \nabla \cdot \sigma + \rho b. \quad (11)$$

where $\rho(\mathbf{x}, t)$ represents the mass density of a point at location \mathbf{x} and time t , $v(\mathbf{x}, t)$ represents the velocity, $a(\mathbf{x}, t)$ the acceleration, $\sigma(\mathbf{x}, t)$ the Cauchy's stress tensor and $b(\mathbf{x}, t)$ the body force at the point. $\nabla \cdot$ and ∇ represent the divergence and gradient operators, respectively.

A continuum body is discretised into a finite number of material points n_p and let \mathbf{x}_p^t represent the current position of point p at time t where $p = (1, 2, \dots, n_p)$. At any given time t , each point will have an associated mass m_p^t , density ρ_p^t , velocity \mathbf{v}_p^t , and stress and strain σ_p^t and ϵ_p^t , respectively, providing a Lagrangian description of the body. In addition the material points also track parameters required by the chosen constitutive model. To obtain the discrete form of the equation, eq. (11) is multiplied by weight function w and integrated over boundary Ω to give

$$\int_{\Omega} \rho w \cdot a \, d\Omega = \int_{\Omega} w \nabla \cdot \sigma \, d\Omega + \int_{\Omega} \rho w b \, d\Omega. \quad (12)$$

After integration by parts, the application of the divergence theorem and the inclusion of Neumann and Dirichlet boundary conditions, the weak form of the equation of motion is given by

$$\int_{\Omega} \rho w \cdot a \, d\Omega = \int_{\partial\Omega} w \cdot \tau \, dS - \int_{\Omega} \nabla w \cdot \rho \sigma^s \, d\Omega + \int_{\Omega} \rho w b \, d\Omega. \quad (13)$$

Where τ represents surface traction, $\rho \sigma^s$ represents the specific stress ($\sigma^s = \sigma/\rho$) necessary for the derivation of discrete equations, and dS and $d\Omega$ represent surface and volume differential respectively. Equation (10) is automatically satisfied as material points have a fixed mass at all times. As the material is discretised into points, the mass density can now be written as

$$\rho(\mathbf{x}, t) = \sum_{p=1}^{n_p} m_p \delta(\mathbf{x} - \mathbf{x}_p^t) \quad (14)$$

Where δ represents the Dirac delta function. Substituting eq. (14) into eq. (13) converts integrals to summation over material points. The coordinates of a material point located within an element is represented at time t as

$$\mathbf{x}_p^t = \sum_{i=1}^{n_n} \mathbf{x}_i^t N_i(\mathbf{x}_p^t) \quad (15)$$

where spatial nodes are represented as \mathbf{x}_i^t such that node number $i = (1, 2, \dots, n_n)$ with n_n representing the number of nodes in the element. The element type governs the applied basis function N_i . Additional variables also share this form of notation. For example, acceleration is given as:

$$\mathbf{a}_p^t = \sum_{i=1}^{n_n} \mathbf{a}_i^t N_i(\mathbf{x}_p^t) \quad (16)$$

as is the weight function and velocity. Substituting eq. (16) and the summation form of the weak form eq. (13), the equation of motion in discretized form is written as

$$\sum_{j=1}^{n_n} m_{ij}^t \mathbf{a}_j^t = \mathbf{f}_i^{\text{int},t} + \mathbf{f}_i^{\text{ext},t}, \quad (17)$$

where internal force vector is represented as

$$\mathbf{f}_i^{\text{int},t} = - \sum_{p=1}^{n_p} m_p \sigma_p^{s,t} \cdot \nabla N_i(\mathbf{x})|_{\mathbf{x}=\mathbf{x}_p^t}, \quad (18)$$

and the external forces is

$$\mathbf{f}_i^{\text{ext},t} = \sum_{p=1}^{n_p} m_p N_i(\mathbf{x}_p^t) \tau_p^{s,t} h^{-1} + \sum_{p=1}^{n_p} m_p \mathbf{b}_p^t N_i(\mathbf{x}_p^t). \quad (19)$$

Which includes the addition of nodal mass matrix m_{ij}^t . The stress at a point is represented by

$$\sigma_p^{s,t} = \sigma^s(\mathbf{x}_p^t, t). \quad (20)$$

The equation of momentum, eq. (11) is a second-order differential equation with respect to time, so it can be solved by using either an explicit integration scheme or an implicit integration scheme. An implicit method involves finding the unknown displacement solution for the current time step by using information from both the current and previous time steps. An implicit time scheme is recommended for slowly applied and propagated stresses [43]. In contrast, an explicit time integration is commonly used to solve for the acceleration term. As the stresses experienced in a Slump-flow test are rapid, an explicit time scheme is chosen for this study.

The stresses in the MPM algorithm can be updated before or after computing the acceleration term and are commonly referred to as separate methods termed updating stress first (USF) or updating stresses last (USL). Bardenhagen [44] observed that

USL performed better than USF, in addition, al Kafaji [43] recommends the use of USL over USF in a granular flow-like simulation as USL dissipates energy in flow problems. However, the authors found that USF offered greater numerical stability with the Bingham constitutive model used in the study. All simulations discussed in this paper, therefore, use USF. In this study the authors developed a Thixotropic Bingham model which is implemented in the CB-GEO MPM code [45], described later in this section.

The choice of basis function, or shape function, N_i can influence the accuracy and numerical stability of the MPM by reducing cell crossing noise. Cell crossing noise is caused by the discontinuity in point properties observed when a point crosses from one element to another. Bardenhagen and Kober [46] developed Generalised Interpolation Material Point (GIMP) to overcome cell crossing noise typically observed in linear MPM by using shape functions that span multiple elements. This GIMP method was implemented in the CB-GEO code based on [47] to minimise cell crossing errors in concrete flow problems. The GIMP was found to be especially effective in reducing the numerical error caused by points entering empty cells, thereby improving the stability of the simulation.

3.1.2. Boundary Conditions

A frictional boundary algorithm is used to describe the interaction between the concrete material points and the surface on which it flows. A description of this friction algorithm is available in Bandara [36], which involves reducing the acceleration of a point based on a Friction Coefficient (FC). The FC in the Slump-Flow test represents the kinetic and static friction between the concrete and the steel plate. It is well documented in the literature that FC is influenced by rheology, mix design (such as cement/water ratio) and surface roughness of the plate. Roussel and Gram [5] describes friction as a key variable for simulating concrete flow. However, a wide variation in the suitable values of FC can be observed in the literature. For simulating concrete with an SF of 800 mm, Deeb et al. [21] recommended a dynamic FC of 0.55. While Djelal et al. [48] reported a FC of 0.06-0.1 for concrete with an SF of 700 mm. For an L-box test, which is similar to the SF test, Hosseinpoor et al. [49] observed good correlation with experimental results for an FC of 0.4. As in these cases, FC is often used as a calibration parameter in simulations of concrete flow.

Bouharoun [50] observed that the volume of cement paste and the amount of superplasticiser within a concrete mix affects the friction at the concrete plate interface. The friction stresses at the interface were observed to increase with increasing paste volume due to the enrichment of the boundary layer caused by the availability of more fines. The greater thickness of the boundary allows more cement grains to be trapped in the roughness of the metal plate. Bouharoun [50] also demonstrated that friction stress, which is proportional to the friction coefficient, decreases with increasing plastic viscosity. In the present study, calibrated FC values between 0.35 and 0.45 are used to represent the friction between Tremie Concrete and the base-plate, as shown in table 1. FC also increases with decreasing plastic viscosity to align with the observations made

in Bouharoun [50].

3.1.3. Geometry

The geometry of the Sump-Flow test in 3D is discretised using approximately 17,000 material points. 4000 points represent the Slump-cone with the remainder representing Tremie Concrete. High density, rigid material points are used to model the Slump-cone to prevent any unwanted outward flow of concrete from the cone. It is important to simulate the cone as it confines the initial flow of concrete, reducing the overall spread. Without the cone, the simulations are not subject to the correct confining forces, producing an unrealistic early geometry of the flow. At the start of the simulation, the cone is raised at a speed of 15 cm s^{-1} so as to raise the cone in 1-3 s as per the BSI [11] guidelines. The background mesh is discretised with 256,000 nodes creating 219,373 hexahedral GIMP elements.

3.2. Constitutive Model

According to Reddy [51], in 3 dimensions, the gradient of the velocity u is a second-order tensor which can be expressed as the matrix \mathbf{L}_{ij} :

$$\mathbf{L}_{ij} = \frac{\partial u_i}{\partial x_j}. \quad (21)$$

\mathbf{L}_{ij} can be decomposed into the sum of a symmetric matrix \mathbf{D}_{ij} and a skew-symmetric matrix \mathbf{W}_{ij} as follows

$$\mathbf{D}_{ij} = \frac{1}{2}(\mathbf{L}_{ij} + \mathbf{L}_{ij}^T) \quad (22)$$

$$\mathbf{W}_{ij} = \frac{1}{2}(\mathbf{L}_{ij} - \mathbf{L}_{ij}^T) \quad (23)$$

where \mathbf{D}_{ij} and \mathbf{W}_{ij} are the rate of deformation tensor:

$$\mathbf{D}_{ij} = \begin{bmatrix} \frac{du_x}{dx} & \frac{1}{2}\left(\frac{du_x}{dy} + \frac{du_y}{dx}\right) & \frac{1}{2}\left(\frac{du_x}{dz} + \frac{du_z}{dx}\right) \\ \frac{1}{2}\left(\frac{du_x}{dy} + \frac{du_y}{dx}\right) & \frac{du_y}{dy} & \frac{1}{2}\left(\frac{du_y}{dz} + \frac{du_z}{dy}\right) \\ \frac{1}{2}\left(\frac{du_x}{dz} + \frac{du_z}{dx}\right) & \frac{1}{2}\left(\frac{du_y}{dz} + \frac{du_z}{dy}\right) & \frac{du_z}{dz} \end{bmatrix} \quad (24)$$

and the vorticity tensor or spin tensor respectively. In the CB-GEO MPM, the strain rate tensor $\dot{\epsilon}$ is calculated as $\mathbf{B}\mathbf{u}$, where \mathbf{B} is the strain-displacement B-matrix [52] to give

$$\dot{\epsilon} = \mathbf{B}\mathbf{u} = \begin{bmatrix} \frac{du_x}{dx} & \left(\frac{du_x}{dy} + \frac{du_y}{dx}\right) & \left(\frac{du_x}{dz} + \frac{du_z}{dx}\right) \\ \left(\frac{du_x}{dy} + \frac{du_y}{dx}\right) & \frac{du_y}{dy} & \left(\frac{du_y}{dz} + \frac{du_z}{dy}\right) \\ \left(\frac{du_x}{dz} + \frac{du_z}{dx}\right) & \left(\frac{du_y}{dz} + \frac{du_z}{dy}\right) & \frac{du_z}{dz} \end{bmatrix} \quad (25)$$

such that the rate of deformation tensor can also be represented as a 6x1 function of the rate of strain

$$\mathbf{D}_{ij} = \left[\dot{\epsilon}_{xx}, \dot{\epsilon}_{yy}, \dot{\epsilon}_{zz}, \frac{1}{2}\dot{\epsilon}_{xy}, \frac{1}{2}\dot{\epsilon}_{yz}, \frac{1}{2}\dot{\epsilon}_{zx} \right]^T. \quad (26)$$

Using the rate of deformation, eq. (1) can be expressed as

$$\boldsymbol{\tau}_{ij} = 2\left(\frac{\tau_0}{\dot{\gamma}} + \mu\right)\mathbf{D}_{ij} \quad \text{if } |\boldsymbol{\tau}_{ij}| \geq \tau_0 \quad (27)$$

where $\boldsymbol{\tau}_{ij}$ is the deviatoric stress tensor and $\mathbf{D}_{ij} = 0$ if $|\boldsymbol{\tau}_{ij}| < \tau_0$. The shear rate $\dot{\gamma}$ can now be described as

$$\dot{\gamma} = (2\mathbf{D}_{ij}\mathbf{D}_{ij})^{1/2}. \quad (28)$$

The total stress σ_{ij} can be calculated from the deviatoric stress tensor, the thermodynamic pressure P and the Dirac Delta function δ_{ij} by:

$$\boldsymbol{\sigma}_{ij} = -P\delta_{ij} + \boldsymbol{\tau}_{ij} \quad (29)$$

where pressure P is

$$P = p_0 - Kd\epsilon_v. \quad (30)$$

Here, p_0 is the initial thermodynamic pressure (calculated as the mean initial stress) $d\epsilon_v$ is the volumetric strain and K is the bulk modulus

$$K = \frac{E}{3(1-2\nu)} \quad (31)$$

In this study, we use a Young's Modulus E of 0.01 MPa [3] and a Poisson's ratio ν of 0.45 to represent a weakly incompressible material. The thermodynamic pressure is calculated at the centre of the MPM cell to minimise pressure oscillations.

Fresh concrete modelled using a viscoplastic Bingham material behaves like a rigid body before yielding, and as a viscous material upon yielding. In order for the material to transition from rigid to viscous, the magnitude of the deviatoric stress tensor must exceed the yield stress. Based on eq. (27), total stresses will remain zero when the material is in the rigid region because the rate of deformation will also be zero. In reality, this is not physically possible as a material in the rigid zone will still exhibit non-zero stresses, despite not flowing. Hence, a modification to this model is needed to allow non-zero stresses to develop before the material yields.

One such modification, or regularisation, is to define the behaviour before and after yield as two separate materials. The most commonly adopted modification is the Bi-viscous model [53], which uses a critical shear rate $\dot{\gamma}_c$ to define the shear rate at which the transition between rigid and viscous behaviour occurs. The Bi-viscous model is written as:

$$\boldsymbol{\tau}_{ij} = \begin{cases} 2\mu_0\mathbf{D}_{ij} & \text{if } |\dot{\gamma}| \leq \dot{\gamma}_c \\ 2\left(\frac{\tau_0}{\dot{\gamma}} + \mu\right)\mathbf{D}_{ij} & \text{otherwise} \end{cases} \quad (32)$$

where μ_0 represents the viscosity of the material in the pre-yield region, and typically has a value three orders of magnitude higher than the dynamic viscosity μ .

The Bi-viscous model offers a clear differentiation between the yielding and pre-yield regions by using a critical yield stress. However, the abrupt discontinuity at the transition between the regions still presents a computational hurdle. An alternative regularising method involves adopting a continuous model which does not have a distinct discontinuity between rigid and plastic regions. The Papanastasiou [54] model represents the most popular of these kinds of continuous models.

The exponential regularisation of the Bingham model often referred to as the Bingham-Papanastasiou model, introduces a parameter m which controls the exponential growth of stress. The 3D representation of this regularisation is:

$$\boldsymbol{\tau}_{ij} = 2 \left[\mu + \frac{\tau_0}{\dot{\gamma}} (1 - e^{-m\dot{\gamma}}) \right] \mathbf{D}_{ij} \quad (33)$$

The larger the regularisation parameter m , the closer the numerical representation will be to the Bingham model in eq. (27). However, any increase in m will also result in a significant increase in the apparent viscosity at low strain rates. Thus, high m values create an unrealistic stiffness which can lead to volumetric locking within MPM. Locking effects in MPM can be mitigated by reducing the number of material points in cells and calculating the volumetric deformation at the centre of the cell [55]. Due to the significant increases in stiffness exhibited by thixotropic concrete and the use of velocity gradient rather than deformation gradient in the MPM implementation, these mitigations were not sufficient to reduce the effect of locking to a suitable level. Franci and Zhang [56] demonstrated how different m values have a marginal impact on the behaviour of a Bingham representation of cement paste but can influence the stability of a model. An m value of 5 reduced the influence of locking on the simulations substantially and is subsequently used in all simulations in this study. For the first time, we propose a new model that combines Roussel's thixotropic equations which describe time-dependent concrete behaviour with a continuous Bingham model by substituting eq. (5) into eq. (33) to give:

$$\boldsymbol{\tau}_{ij} = 2 \left[\mu + \frac{(1 + \lambda_0 e^{-\alpha \dot{\gamma} t}) \tau_0}{\dot{\gamma}} (1 - e^{-m\dot{\gamma}}) \right] \mathbf{D}_{ij}. \quad (34)$$

This model will be referred to as the the Papanastasiou-Roussel Bingham (PR-Bingham) model for the remainder of this paper. Equation (34) is valid for all strain-rates and degrees of concrete thixotropy. However, for computational purposes, there is still a need to define a point at which thixotropy increases whilst the material is at rest, and a point where thixotropy begins to decrease as the material flows. In this work, a critical shear rate, $\dot{\gamma}_c$, is used to define a yield point, similar to the approach taken by Beverly and Tanner [53]. In the model adopted here, any material with a shear rate below the critical shear rate is considered to be at rest, allowing thixotropy to build. However, material at these low shear rates may still exhibit a degree of movement as a result of using the Papanastasiou model. From an engineering perspective the material can still be considered at rest even with a small, often negligible, degree of deformation as noted by Franci and Zhang [56].

Roussel et al. [57] suggested the use of a stopping criterion which allows for the definition of the final shape of the free surface of the material regardless of any continued, negligible deformation. This criterion has taken the form of a flow-cut off time in previous studies [6], where it is assumed that any flow occurring after this point is a result of the limitations of the constitutive model. The stopping criterion used in this study is 20 s of flow time, in line with that used by Fierenkothen [6]. This

Algorithm 1: Thixotropic Bingham algorithm

```

if ( $\dot{\gamma} \cdot \dot{\gamma}$ ) > ( $\dot{\gamma}_{critical} \cdot \dot{\gamma}_{critical}$ ) ;
then
  if ( $\lambda_{n-1} > 0$ );
  then
     $\lambda_n = \lambda_{n-1} e^{-\alpha \dot{\gamma} \delta t}$  ;
    if ( $\lambda_n > 0$ );
    then
       $\tau_{0temp} = (1 + \lambda_n) \cdot \tau_0$ 
       $\boldsymbol{\tau}_{ij} = 2 \left[ \mu + \frac{\tau_{0temp}}{\dot{\gamma}} (1 - e^{-m\dot{\gamma}}) \right] \mathbf{D}_{ij}$ 
       $rt = 0$ 
    else
       $\lambda_n = 0$ ;
       $\boldsymbol{\tau}_{ij} = 2 \left[ \mu + \frac{\tau_0}{\dot{\gamma}} (1 - e^{-m\dot{\gamma}}) \right] \mathbf{D}_{ij}$ 
       $rt = 0$ 
    end
  else
     $\boldsymbol{\tau}_{ij} = 2 \left[ \mu + \frac{\tau_0}{\dot{\gamma}} (1 - e^{-m\dot{\gamma}}) \right] \mathbf{D}_{ij}$ 
     $rt = 0$  ;
  end
else
  if  $\lambda > 0$  then
    |  $apparent\ rt = \frac{\lambda * \tau_0}{A_{thix}}$ 
  else
    |  $apparent\ rt = rt$ 
  end
   $apparent\ rt += \delta t$ ;
   $\tau_{0temp} = \tau_0 + (A_{thix} * apparent\ rt)$  ;
   $\lambda_n = \left( \frac{\tau_{0temp}}{\tau_0} \right) - 1$  ;
   $\boldsymbol{\tau}_{ij} = 2 \left[ \mu + \frac{\tau_{0temp}}{\dot{\gamma}} (1 - e^{-m\dot{\gamma}}) \right] \mathbf{D}_{ij}$ 
end

```

Figure 6: The Papanastasiou-Roussel Bingham (PR-Bingham) algorithm implemented in CB-GEO MPM.

represents more than the maximum SF time for all concretes presented in fig. 4 [13, 14].

Figure 6 shows the Algorithm used to build up thixotropic stresses in CB-GEO MPM in accordance with eq. (34), where δt represents the length of a time-step (1.0×10^{-4} s), λ_{n-1} the flocculation state of the previous time-step, and the addition of a yield criterion in the form of a critical shear rate. All results in the following section use this algorithm to calculate the stress state of the material over time.

An appropriate way to characterise a thixotropic system is to use the hysteresis loop of the flow curve, representing an applied shear stress (upward) followed by a relaxing of the stress (downward) [58]. Figure 7 represents a 1D single hysteresis loop analogous to fig. 6, demonstrating how the thixotropy multiplier λ increases the yield stress after a period of rest and dissipates to 0 during shearing, resulting in a hysteresis loop.

A parametric study is performed to understand the effect of the model parameters (τ_0 , μ , α , A_{thix} , m and rest time) on the

Table 1: MPM input parameters of Mixes A-C, based on [13, 14]

	$\tau_{0,dynamic}$ [Pa]	μ [Pa · s]	A_{thix} [Pa · s ⁻¹]	SF ₀ ± 30 [mm]	SF ₂₄₀ ± 30 [mm]	FC
Mix A	54	35.8	1.3	590	575	0.35
Mix B	61	29	1.8	550	530	0.45
Mix C	130	30.2	2.9	500	485	0.43

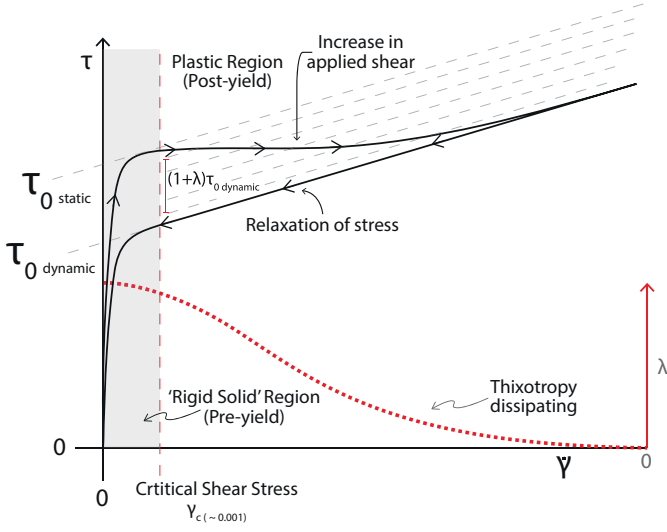


Figure 7: 1D Bi-viscous Thixotropic Bingham hysteresis loop

shear stress and the thixotropic multiplier λ following a 100 s rest period. The results of the parametric study are presented in fig. 8. An increase in τ_0 causes an upward translation of the shear stress intercept, and a downward translation of λ as the constant increase in yield stress over time is now proportionately smaller than the initial yield stress. Increasing μ sees the gradient of the $\tau/\dot{\gamma}$ curve steepen, creating higher stresses at lower shear rates. Changes in rest time and A_{thix} both increase the $\tau_{0,static}$ reached after a period of rest. A larger α value causes a reduction in the time required for the elevated $\tau_{0,static}$ to reduce to the $\tau_{0,dynamic}$ during shearing. Finally, as discussed previously, a larger m results in a model closer to the true Bingham model, but at a cost of increasing the stresses at lower shear rates.

3.3. Calibration of input parameters

To demonstrate the capability of the developed PR-Bingham MPM model in simulating Tremie Concrete, the results of numerical simulations are compared against experimental slump-flow tests [13, 14]. Dynamic yield stress, plastic viscosity, A_{thix} , SF_0 and SF_{240} values were obtained from an EFFC and DFI data-set [13, 14] of concrete tests performed on Tremie Concrete from numerous European and North American sites. Three concretes from this data set, referred to as Mix A-C, are chosen based on the range of concrete properties they represent. The model parameters for Mixes A-C used in this study are shown in table 1, where SF_0 and SF_{240} represent the measured SF in mm for 0 seconds of rest and 240 seconds of rest, respectively, for the physical test.

Mix A is a low yield stress, high viscosity concrete with a low level of thixotropy. This produces a SF of almost 600 mm which is in the upper range of acceptability. Mix B has a similar yield stress to Mix A, but has a significantly lower viscosity, resulting in lower FC requirement and a mid-range SF of 550 mm. Mix B also has a slightly higher level of thixotropy, as represented by the increase in A_{thix} of 0.5 from Mix A. Finally, Mix C has a significantly higher yield stress, resulting in a SF of only 500 mm, near the lower limit of acceptability. Mix C also has a significantly higher degree of thixotropy, with an A_{thix} of 2.9. The SF behaviour of the three different mixes and their comparison with the physical experiments are presented in the following section.

Furthermore, we evaluate the influence of incorporating thixotropy to accurately represent concrete. A rest time of 240 s is introduced in the PR-Bingham algorithm to induce time-dependent changes in the concrete as described in fig. 6. Depending on the duration of the rest time, an appropriate increase in the λ value causes an increase in the shear stress to $\tau_{0,static}$.

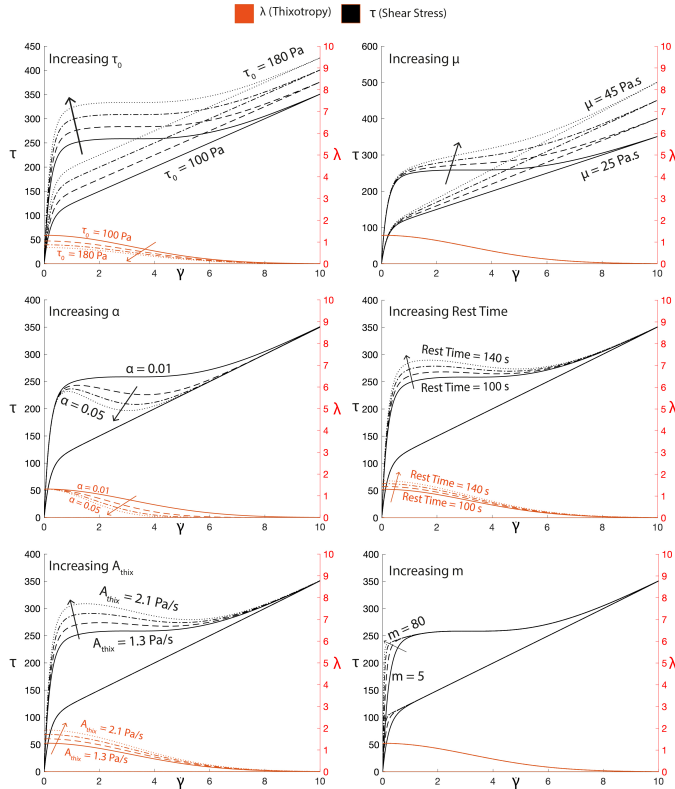


Figure 8: Parametric study of thixotropic algorithm. Blue represents the shear stress and orange the thixotropic multiplier λ .

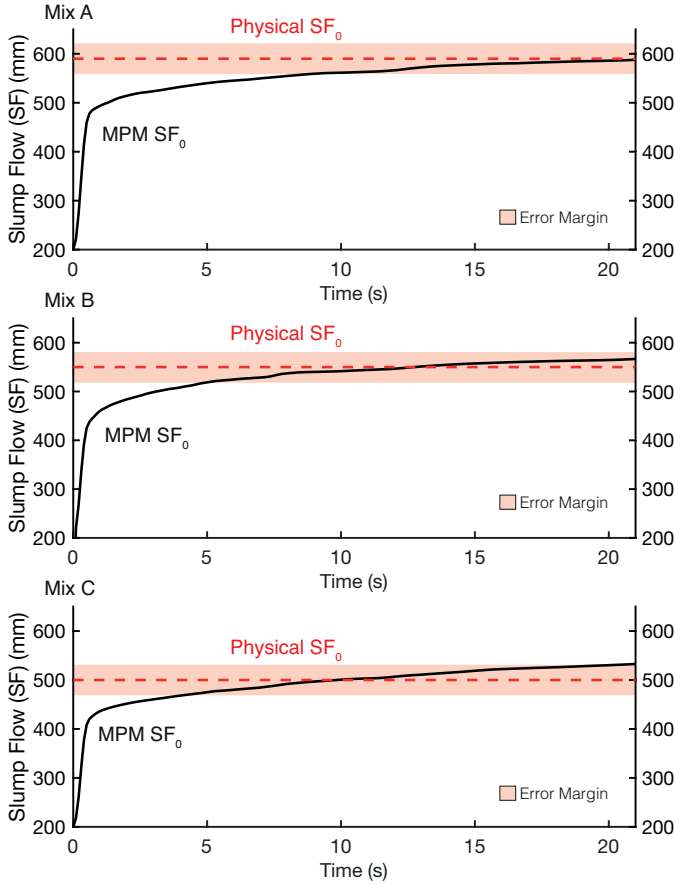


Figure 9: Evolution of MPM simulated SF_0 over time for each concrete mix, dashed line indicates the physical SF_0 and MPM simulated SF_0 from table 1.

4. Results and Discussion

4.1. Dynamic Property Simulations

Figure 9 shows the time-evolution of the Slump-flow spread in mm for Mixes A-C (see table 1) where no rest time is present. For Mix A, a highly viscous low yield stress concrete, the MPM SF_0 reaches the corresponding Physical SF_0 around 18 s. This is expected for a high viscosity concrete like Mix A. The MPM simulations of Mixes B and C reach the physical SF at approximately 10 s and 12 s respectively, as both mixes have a lower viscosity in comparison to Mix A. The MPM SF_0 for Mixes A and B continues to grow at a negligible level after reaching the physical SF_0 due to low shear deformation caused by PR-Bingham model. Despite this continued growth, the MPM SF_0 for mixes A and B remain within the margin of error [59]. The MPM SF_0 for Mix C does continue to grow at a higher rate after reaching the physical SF_0 , but still reached a stable level within the physical SF_0 margin of error. The continued growth of Mix C is due to the constant deformation at a low shear rate characteristic of the PR-Bingham model with larger yield stress.

Figure 10 shows the three-dimensional isometric view of the evolution of all three mixes as they leave the cone at 0.3 s and the final shape at 20 s. Figure 10 shows a clear difference in spread diameter for the mixes at 0.3 s. The final spread are

Table 2: Difference in Slump-flow following a period of rest for physical tests and MPM simulations.

	ΔSF (mm)		ΔSF (% of SF_0)	
	Physical	MPM	Physical	MPM
Mix A	15	105	2.6	18.0
Mix B	20	94	4.0	18.8
Mix C	15	98	3.1	20.2

significantly different, but the three mixes maintain a uniform shape and thickness.

The good level of correlation between the physical and numerical SF_0 indicates that the PR-Bingham model developed in the MPM framework is capable of modelling the rheological behaviour of Tremie Concrete.

4.2. Thixotropic Simulations

The time dependent thixotropic behaviour of Tremie concrete is simulated by introducing a rest time to build the yield stress of Tremie Concrete. Figure 11 compares the evolution of the MPM SF_{240} and the Physical SF_{240} for Mixes A-C. After an initial rest period of 240 s all three concretes fall short of reaching the final experimental SF by approximately 60-80 mm.

The difference in the SF run-out with and without the initial rest time of 240 s is defined as ΔSF . The ΔSF values for the MPM simulations are summarised in table 2 for Mixes A-C, showing an approximately 100 mm change in the SF following a 240 s rest. Conversely, as discussed earlier in this paper, the experimental ΔSF values for Mixes A-C measured in the physical tests are significantly lower, ranging between 15 mm and 20 mm. In the PR-Bingham model, the values of A_{thix} over 1 cause an increase in the yield stress of over 240 Pa during a rest period of 240 s. Figure 2 shows that an increase in yield stress of over 240 Pa should yield a significant ΔSF , more than the observed 15-20 mm difference. The ΔSF observed in MPM simulations are still lower than what is the expected given the generalised empirical relationship between SF and τ_0 for a concrete with a yield stress of >250 Pa, but is closer to the expected behaviour than the ΔSF Physical values.

As discussed in section 2.2, Kraenkel and Gehlen [13], Feys and Khayat [14] could not find a consensus on why the physical Slump-flow test could not accurately represent thixotropic concrete, just that it was inadequate at doing so. This is supported by the small ΔSF physical values in table 2. Interestingly, the MPM simulations appear to capture a behaviour closer to the expected flow behaviour, with large ΔSF values reported in the MPM simulations. It is possible that the simulations overcome some physical artefacts that prevents the physical Slump-Flow test from representing the difference in the flow behaviour of thixotropic concrete. The MPM simulations also align better with the rheometer measurements of Mixes A-C reported by [13, 14], which describes large increases in yield stress (material stiffness) over short rest periods, as noted by the high A_{thix} values in table 1.

It is possible that high shear rates during the slump-flow test remove a significant portion of thixotropy, preventing the test

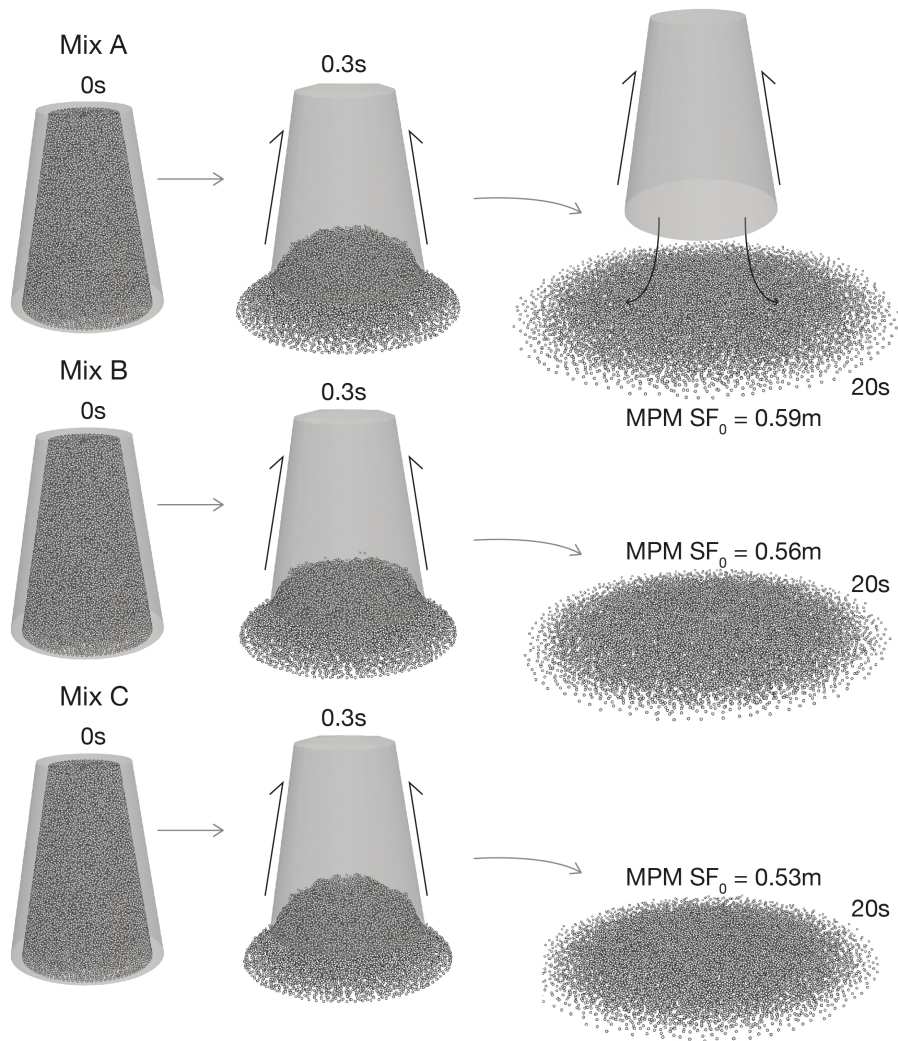


Figure 10: Time evolution of Slump-flow test for all mixes. From top to bottom: Mix A, Mix B and Mix C

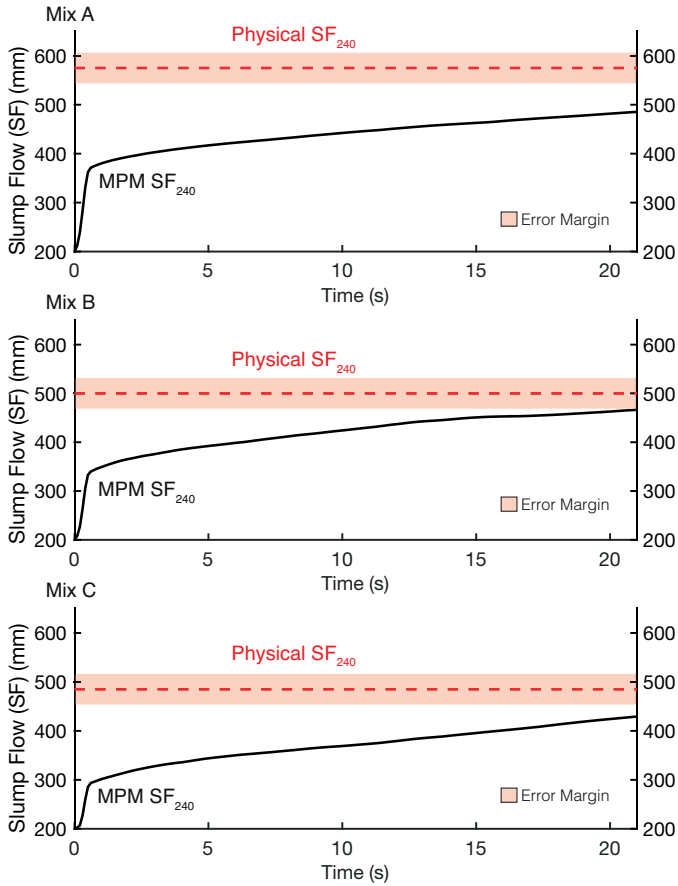


Figure 11: Evolution of MPM simulated SF_{240} over time for each concrete mix, dashed line indicates the physical SF_{240} from table 1.

from accurately representing thixotropic concrete. This proposition can be disproved by examining the mean average shear rate occurring during a Slump-flow test, fig. 13a. In Mix A, the peak shear rate is approximately 12 s^{-1} and 9 s^{-1} for 0 s rest and 240 s rest, respectively. However, the slump-flow test experiences this peak shear rate only for a very short duration and is not sufficient to dissipate the large amount thixotropy developed at rest. The shear-stress that develops as the rate of SF spreading declines will also not be sufficient to remove a significant portion of thixotropy. This can be further supported by the time required to reduce static shear stresses to dynamic in a rheometer, which is around 10 s and requires a constant shear-rate of up to 12 s^{-1} [28]. The Slump-flow test does not experience shear rates high enough to dissipate much thixotropy. The implication of this observation is that if the slump flow test does not experience enough shear stresses to break down thixotropy, then the ΔSF for the physical test should be much larger, as it is with the MPM ΔSF . This supports the observation that MPM is not only capable of simulating dynamic concrete properties, but also static properties of thixotropic concrete.

The thixotropic parameter λ directly controls the increase in the yield stress. Figure 12 shows the dissipation of λ with time for all mixes. At 20 s of flow-time, the result of the relatively low shear rates experienced by the concrete has prevented any notable dissipation of thixotropy. As the lowest shear rates are experienced close to the centre of the spread, the thixotropic dissipation has occurred the least in these areas. For all three mixes shown in fig. 12, the centre regions display higher λ values than the edges. This again supports the argument that the Slump-flow test is not capable of dissipating a significant amount of thixotropy.

Figure 13b reveals the rate of dissipation of the mean λ over time during the test for all three mixes. It can be noted here that from approximately 3 s of flow time, the gradient of the slope remains relatively constant. Therefore, the bulk of thixotropy dissipation is likely to happen within the initial period of the test.

One final piece of evidence suggesting the inability of the Slump-flow test to dissipate thixotropy is presented by fig. 14a. Here, a simulation is conducted where all starting properties are equal to Mix A MPM SF_0 , apart from the starting yield stress, which has been increased to 367 Pa. This value is equal to the static yield stress of Mix A following a 240 s rest. The final SF measurements and the evolution of SF are almost identical, as shown by the overlain curve (dashed line) of Mix A MPM SF_{240} . This suggests that the thixotropic effects developed at rest within concrete are not dissipating, resulting in an elevated yield stress that affects the final run-out distance.

In the previous section of this paper, a parametric study (fig. 8) of the PR-Bingham parameters was shown. The parameter, α , influenced the rate at which thixotropy would dissipate following the application of stress. For the MPM simulations presented, an α of 0.01 was used, to be inline with experimental observations from a rheometer and observations in the literature. To provide continued evidence that the Slump-flow test does not dissipate thixotropy significantly, fig. 14b demonstrates the effect on thixotropy dissipation for two different val-

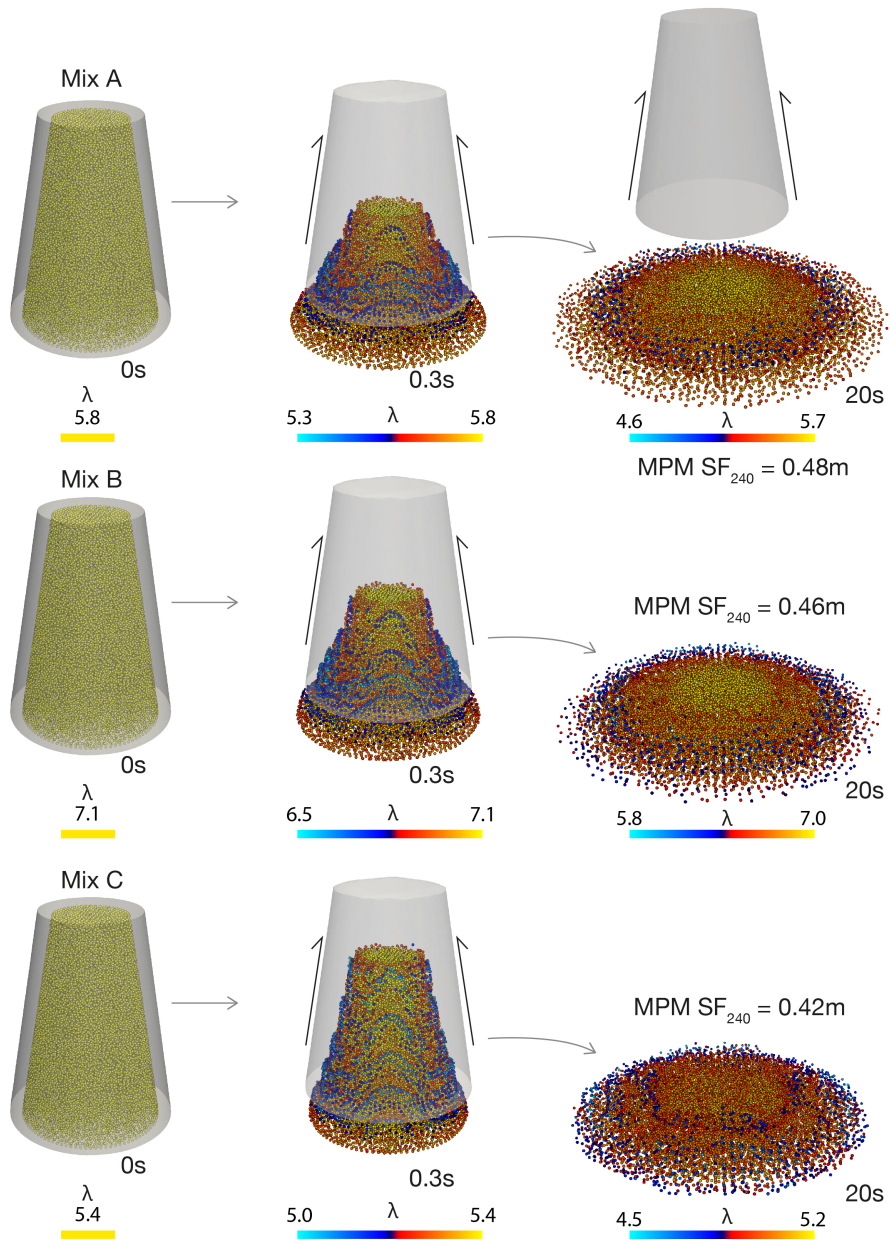


Figure 12: Time evolution of Slump-flow test for all mixes following a rest period of 240 s. From top to bottom: Mix A, Mix B and Mix C

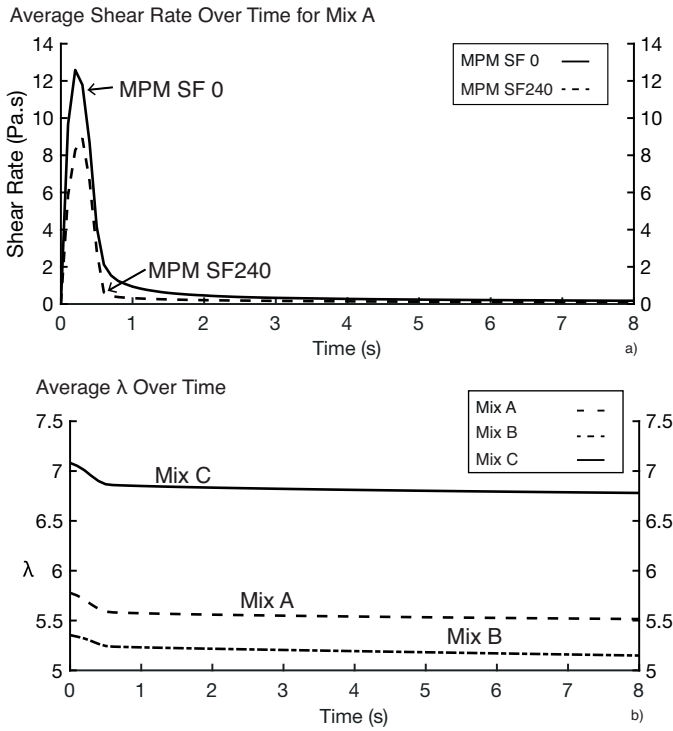


Figure 13: A) Mean average shear rate for Mix A during the Slump-Flow test for 0s rest and 240s rest B) Time evolution of λ for all mixes following a rest period of 240 s. From top to bottom: Mix B, Mix A and Mix C

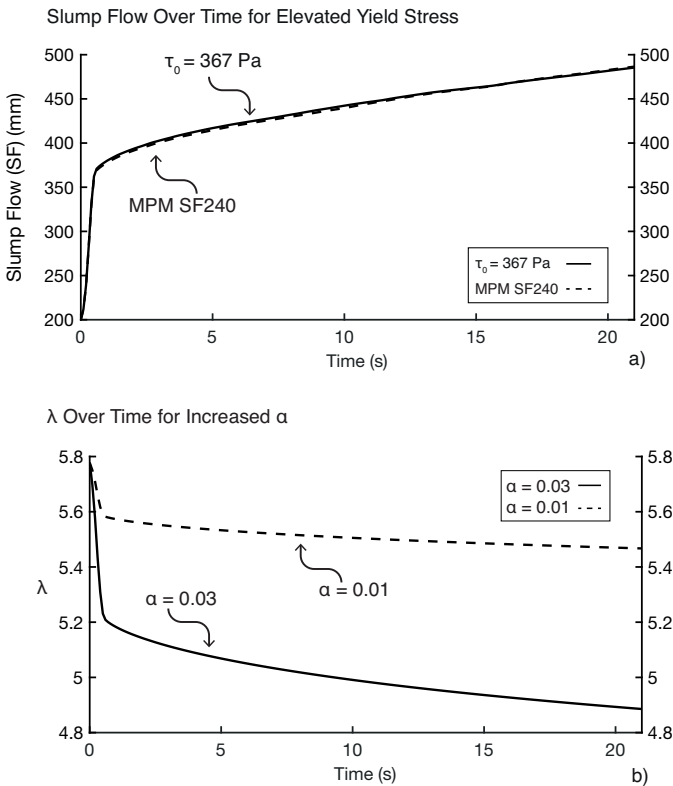


Figure 14: A) Time evolution of Slump-flow test for Mix A following a rest period of 240 s and from 0 s rest but with a starting yield stress equal to Mix A at 240 s rest. B) Effect of alpha increase on dissipation of λ .

ues of alpha ($\alpha = 0.03$ and 0.01). What can be observed, for Mix A, is that an increase in alpha from 0.01 to 0.03 causes a reduction of thixotropic multiplier λ from 5.7 to approximately 4.8, as opposed to approximately 5.4 for an α of 0.01. While this does represent an increase in thixotropy dissipation, the final SF was within 5 mm of Mix A MPM SF₂₄₀. Thus, even concrete significantly more susceptible to thixotropic dissipation still retains an increased stiffness during the Slump-flow test.

The MPM framework with PR-Bingham model has been successful in offering insights into the flow behaviour of thixotropic concrete. The model suggests that the flow of concrete should be impacted by its thixotropic properties on a greater scale than empirical testing seems to suggest, and in line with observations from a rheometer.

5. Conclusion

The objective of this paper was to model thixotropic Tremie Concrete for the first time, using the Material Point Method to explore the challenges of testing concrete and how numerical modelling can provide unique insights into concrete flow behaviour. We have observed the following:

- The new MPM PR-Bingham model that combines the Papanastasiou-Bingham model with Roussel's simplified thixotropy equations is successful in accurately representing concrete flow behaviour in both dynamic and thixotropic conditions.
- MPM simulations of weakly incompressible materials such as tremie concrete results in numerical errors such as volume locking. Volume locking in weakly compressible flows are reduced using higher order shape functions, setting the m parameter in the PR-Bingham model to a low number and using reduced integration for pressure calculations.
- A comprehensive calibration and material property assessment procedure, outlined in this paper, can be used to verify simulated Tremie Concrete.
- Finally, a comparison of physical and numerical results of the Slump-Flow test for thixotropic concrete reveal for the first time, a decline in concrete workability during the Slump-Flow test for simulated concrete, in line with theoretical predictions, that was not captured by the physical version of the test.

6. Acknowledgements

This work was funded through an EPSRC ICASE award (Ref: 1769998) in partnership with industry partner ARUP. The authors thank the CB-GEO computational geomechanics research group for assistance in preparing the simulations. The authors would also like to acknowledge the EFFC and DFI research groups for providing data sets with which to work.

References

- [1] EFFC, DFI, Guide to Tremie Concrete for Deep Foundations, 2018.
- [2] N. Roussel, A thixotropy model for fresh fluid concretes: Theory, validation and applications, *Cement and Concrete Research* 36 (2006) 1797–1806.
- [3] N. Roussel, G. Ovarlez, S. Garrault, C. Brumaud, The origins of thixotropy of fresh cement pastes, *Cement and Concrete Research* 42 (2012) 148–157.
- [4] A. Thorp, C. Wilkes, D. Nicholson, M. Bryan, Recent Experience with Tremie Concrete Properties and Testing, *Proceeding of the 2018 DFI-EFFC International Conference on Deep Foundations and Ground Improvement, Rome, Italy* (2018).
- [5] N. Roussel, A. Gram, Simulation of fresh concrete flow, *RILEM State-of-the-Art Reports* 15 (2014).
- [6] C. Fierenkothen, Numerische Simulationen und Laborversuche zur Ausbreitung von Frischbeton in Bohrpfehlen (Berichte des Lehr- und Forschungsgebietes Geotechnik, Nr. 38), 2019.
- [7] K. Vasilic, A. Gram, J. E. Wallevik, Numerical simulation of fresh concrete flow: insight and challenges, *RILEM Technical Letters* 4 (2019) 57–66.
- [8] N. Roussel, J. Spangenberg, J. Wallevik, R. Wolfs, Numerical simulations of concrete processing: from standard formative casting to additive manufacturing, *Cement and Concrete Research* 135 (2020) 106075.
- [9] D. Sulsky, Z. Chen, H. L. Schreyer, A particle method for history-dependent materials, *Computer methods in applied mechanics and engineering* 118 (1994) 179–196.
- [10] D. Sulsky, S.-J. Zhou, H. L. Schreyer, Application of a particle-in-cell method to solid mechanics, *Computer Physics Communications* 87 (1995) 236–252.
- [11] BSI, BS EN 12350-8:2019, Self Compacting concrete - Slump-flow test, Standard, The British Standards Institute, 2019.
- [12] ICE, Specification for piling and embedded retaining walls / Institution of Civil Engineers., third edit ed., 2017.
- [13] T. Kraenkel, C. Gehlen, Rheology and Workability Testing of Deep Foundation Concrete in Europe and the US. Research Report No. 20-F-0107, Chair of Materials Science and Testing, Centre for Building Materials, Technical University of Munich (2018).
- [14] D. Feys, K. H. Khayat, Testing Concrete For Deep Foundations, 2018.
- [15] J. E. Wallevik, Relationship between the Bingham parameters and slump, *Cement and Concrete Research* 36 (2006) 1214–1221.
- [16] N. Roussel, P. Coussot, Fifty-cent rheometer for yield stress measurements: From slump to spreading flow, *Journal of Rheology* 49 (2005) 705–718.
- [17] A. W. Saak, H. M. Jennings, S. P. Shah, A generalized approach for the determination of yield stress by slump and slump flow, *Cement and concrete research* 34 (2004) 363–371.
- [18] G. H. Tattersall, P. F. G. Banfill, *The rheology of fresh concrete.*, Pitman, London, 1983.
- [19] N. Roussel, *Understanding the rheology of concrete*, Elsevier, 2011.
- [20] D. Feys, K. H. Khayat, R. Khatib, How do concrete rheology, tribology, flow rate and pipe radius influence pumping pressure?, *Cement and Concrete Composites* 66 (2016) 38–46.
- [21] R. Deeb, S. Kulasegaram, B. L. Karihaloo, 3d modelling of the flow of self-compacting concrete with or without steel fibres. part i: slump flow test, *Computational Particle Mechanics* 1 (2014) 373–389.
- [22] I. Nielsson, O. H. Wallevik, Rheological evaluation of some empirical test methods preliminary results, in: *Third international RILEM symposium, RILEM Pub. PRO, volume 33, 2003*, pp. 59–68.
- [23] Y. Tanigawa, H. Mori, Analytical study on deformation of fresh concrete, *Journal of Engineering Mechanics* 115 (1989) 493–508.
- [24] Y. Qian, S. Kawashima, Distinguishing dynamic and static yield stress of fresh cement mortars through thixotropy, *Cement and Concrete Composites* 86 (2018) 288–296.
- [25] T. Lecompte, A. Perrot, Non-linear modeling of yield stress increase due to scc structural build-up at rest, *Cement and Concrete Research* 92 (2017) 92–97.
- [26] N. Roussel, M. R. Geiker, F. Dufour, L. N. Thrane, P. Szabo, Computational modeling of concrete flow: general overview, *Cement and Concrete research* 37 (2007) 1298–1307.
- [27] A. Papo, The thixotropic behavior of white portland cement pastes, *Cement and Concrete Research* 18 (1988) 595–603.
- [28] E. P. Koehler, D. W. Fowler, Development of a portable rheometer for fresh portland cement concrete, Technical Report, International Center for Aggregates Research, 2004.
- [29] O. H. Wallevik, D. Feys, J. E. Wallevik, K. H. Khayat, Avoiding inaccurate interpretations of rheological measurements for cement-based materials, *Cement and Concrete Research* 78 (2015) 100–109.
- [30] D. Feys, R. Cepuritis, S. Jacobsen, K. Lesage, E. Secieru, A. Yahia, Measuring rheological properties of cement pastes: most common techniques, procedures and challenges, *RILEM technical letters* 2 (2018) 129–135.
- [31] N. Roussel, Rheology of fresh concrete: from measurements to predictions of casting processes, *Materials and Structures* 40 (2007) 1001–1012.
- [32] V. Mechtcherine, A. Gram, K. Krenzer, J.-H. Schwabe, S. Shyshko, N. Roussel, Simulation of fresh concrete flow using discrete element method (dem): theory and applications, *Materials and Structures* 47 (2014) 615–630.
- [33] K. Vasilic, W. Schmidt, H.-C. Kühne, F. Haamkens, V. Mechtcherine, N. Roussel, Flow of fresh concrete through reinforced elements: experimental validation of the porous analogy numerical method, *Cement and Concrete Research* 88 (2016) 1–6.
- [34] R. De Schryver, K. El Cheikh, K. Lesage, G. De Schutter, Cfd implementation of time-dependent behaviour: application for concrete pumping, in: *Symposium on Concrete Modelling (CONMOD2018), RILEM Publications, 2018*, pp. 122–130.
- [35] K. K. Soundararajan, Multi-scale multiphase modelling of granular flows, Ph.D. thesis, University of Cambridge, 2015.
- [36] S. S. Bandara, Material Point Method to simulate Large Deformation Problems in Fluid-saturated Granular Medium, Ph.D. thesis, University of Cambridge, 2013.
- [37] K. Soga, E. Alonso, A. Yerro, K. Kumar, S. Bandara, Trends in large-deformation analysis of landslide mass movements with particular emphasis on the material point method, *Géotechnique* 66 (2015) 248–273.
- [38] A. Rohe, D. Liang, Modelling large deformation and soil–water–structure interaction with material point method: Briefing on mpm2017 conference, *Journal of Hydrodynamics, Ser. B* 29 (2017) 393–396.
- [39] S. Bandara, K. Soga, Coupling of soil deformation and pore fluid flow using material point method, *Computers and geotechnics* 63 (2015) 199–214.
- [40] B. Wang, P. J. Vardon, M. A. Hicks, Z. Chen, Development of an implicit material point method for geotechnical applications, *Computers and Geotechnics* 71 (2016) 159–167.
- [41] X. Zhang, Z. Chen, Y. Liu, *The Material Point Method: A Continuum-based Particle Method for Extreme Loading Cases*, Academic Press, 2016.
- [42] Z. Chen, R. Brannon, An evaluation of the material point method, *Sandia National Laboratories (SAND2002-0482)* (2002).
- [43] I. K. J. al Kafaji, Formulation of a dynamic material point method (MPM) for geomechanical problems, 2013.
- [44] S. G. Bardenhagen, Energy conservation error in the material point method for solid mechanics, *Journal of Computational Physics* 180 (2002) 383–403.
- [45] K. Kumar, J. Salmond, S. Kularathna, C. Wilkes, E. Tjung, G. Biscontin, K. Soga, Scalable and modular material point method for large-scale simulations, *arXiv preprint arXiv:1909.13380* (2019).
- [46] S. G. Bardenhagen, E. M. Kober, The generalized interpolation material point method, *Computer Modeling in Engineering and Sciences* 5 (2004) 477–496.
- [47] N. Pruijn, The improvement of the material point method by increasing efficiency and accuracy, 2016.
- [48] C. Djelal, Y. Vanhove, A. Magnin, Tribological behaviour of self compacting concrete, *Cement and concrete research* 34 (2004) 821–828.
- [49] M. Hosseinpoor, K. H. Khayat, A. Yahia, Numerical simulation of self-consolidating concrete flow as a heterogeneous material in L-Box set-up: Effect of rheological parameters on flow performance, *Cement and Concrete Composites* 83 (2017) 290–307.
- [50] S. Bouharoun, Friction behaviour of fresh concrete in the vicinity of formwork, *Journal of the South African Institution of Civil Engineering* 55 (2013) 10 – 17.
- [51] J. N. Reddy, *An introduction to continuum mechanics*, Cambridge university press, 2007.
- [52] O. C. Zienkiewicz, R. L. Taylor, *The finite element method for solid and structural mechanics*, Elsevier, 2005.

- [53] C. Beverly, R. Tanner, Numerical analysis of three-dimensional bingham plastic flow, *Journal of Non-Newtonian Fluid Mechanics* 42 (1992) 85 – 115.
- [54] T. C. Papanastasiou, Flows of materials with yield, *Journal of Rheology* 31 (1987) 385–404.
- [55] W. M. Coombs, T. J. Charlton, M. Cortis, C. E. Augarde, Overcoming volumetric locking in material point methods, *Computer Methods in Applied Mechanics and Engineering* 333 (2018) 1–21.
- [56] A. Franci, X. Zhang, 3d numerical simulation of free-surface bingham fluids interacting with structures using the pfem, *Journal of Non-Newtonian Fluid Mechanics* 259 (2018) 1–15.
- [57] N. Roussel, A. Gram, M. Cremonesi, L. Ferrara, K. Krenzer, V. Mechtcherine, S. Shyshko, J. Skocec, J. Spangenberg, O. Svec, L. N. Thrane, K. Vasilic, Numerical simulations of concrete flow: A benchmark comparison, *Cement and Concrete Research* 79 (2016) 265 – 271.
- [58] L. Baltazar, F. Henriques, M. Cidade, Rheology of natural hydraulic lime grouts for conservation of stone masonry—influence of compositional and processing parameters, *Fluids* 4 (2019) 13.
- [59] W. Long, K. Khayat, F. Xing, Repeatability of workability test methods of self-consolidating concrete, *Advanced Materials Research* 168-170 (2010) 1981–1986.